scientific reports

OPEN

Competitive adsorption of CO$_2$, N$_2$, and CH$_4$ in coal-derived asphaltenes, a computational study

Farshad Mirzaee Valadi[1,5], Mohammad Pasandideh-Nadamani[2,5], Mozafar Rezaee[3,5], Abdolhalim Torrik[4,5], Mohammad Mirzaie[1] & Ayoob Torkian[1✉]

Greenhouse gases are major contributors to global warming, and their concentration is increasing due to the widespread use of fossil fuels. Coal bed methane (CBM) offers a potential solution to this issue. However, the gas adsorption mechanisms of CBM, particularly in the context of coal-derived asphaltenes, are not fully understood. This study provides a comprehensive theoretical investigation of the competitive adsorption of carbon dioxide (CO$_2$), methane (CH$_4$), and nitrogen (N$_2$) in the processes of CO$_2$- and N$_2$-enhanced coalbed methane recovery, with a focus on coal-derived asphaltenes functionalized with CH$_4$, NH, O, and S groups. Using the Grand Canonical Monte Carlo (GCMC) simulation method and performing Molecular Dynamics (MD) simulations, we studied the adsorption process. To investigate the electronic effects and nature of the interactions, we performed density functional theory (DFT) calculations. The adsorption energy values and non-covalent interactions (NCI) for the adsorption of gases signify the physical adsorption (van der Waals interaction), with CO$_2$ exhibiting the highest (absolute) adsorption energy. The Monte Carlo results indicated that elevated temperatures led to a reduction in adsorption capacity. Coal-derived asphaltenes demonstrated greater selectivity for CO$_2$ compared to CH$_4$ and N$_2$ in competitive adsorption, especially at elevated temperatures. Our findings highlight the significant potential of our asphaltene model, not only in mitigating CO$_2$ greenhouse gas emissions but also in recovering CH$_4$, which is a valuable resource.

Greenhouse gases are a major contributor to the increase in Earth's temperature. This increase can lead to destructive changes on a global scale, such as the melting of natural glaciers, rising sea levels, tropical storms, climate change, and ocean acidification. As such, the Kyoto Protocol was established in 1997 with the aim of reducing greenhouse gas emissions. This protocol introduces six greenhouse gases: CO$_2$, CH$_4$, nitrous oxide, HFCs, PFCs, and sulfur hexafluoride. Among these gases, CO$_2$ is the most concerning because it is the most abundant of the six gases and has the largest contribution to climate change and global warming. China is the largest energy consumer and produces the highest amount of CO$_2$ globally, with a 30% share of the total emissions[1,2]. It is widely acknowledged that CO$_2$ concentrations are continuously increasing in the atmosphere, primarily due to the use of fossil fuels for energy generation. Currently, fossil fuels supply over 80% of the world's commercial energy[3,4]. A potent approach to combat climate change and global warming is to utilize coal bed methane (CBM)[5,6]. Coal bed methane (CBM), a significant source of unconventional natural gas worldwide, mainly consists of substantial amounts of CH$_4$, minimal quantities of CO$_2$ and N$_2$, and trace amounts of other gases[7,8]. Numerous techniques have been employed to enhance CBM extraction, and gas injection is one of the most important, straightforward, and cost-effective approaches[9,10]. Gas injection is a valuable method for enhancing CH$_4$ recovery, while also providing a practical solution for CH$_4$ disposal and maintaining tank pressure. In a gas-injection-enhanced coalbed methane recovery project, gas is injected into deep, unextractable coal seams, and the resulting CH$_4$ is recovered for use as fuel or clean gas[11,12]. CO$_2$ and N$_2$ are commonly selected as injection

[1]Water and Energy Research Center, Sharif University of Technology, Tehran, Iran. [2]Department of Chemistry, University of Mazandaran, Babolsar, Mazandaran, Iran. [3]Department of Chemistry, Iran University of Science and Technology, Tehran, Iran. [4]Department of Physical and Computational Chemistry, Shahid Beheshti University, Tehran, Iran. [5]These authors contributed equally: Farshad Mirzaee Valadi, Mohammad Pasandideh-Nadamani, Mozafar Rezaee and Abdolhalim Torrik. ✉email: torkian@sharif.edu

gases to enhance CBM recovery because of their favorable structural characteristics for competitive adsorption with CH_4 as well as their easy accessibility[11,13]. This strategy offers numerous benefits, such as preventing mine explosions, enhancing CH_4 recovery and utilization, utilizing abundant resources, lowering atmospheric CO_2 concentration, mitigating global warming, and achieving high efficiency. Therefore, CBM mining has become a popular topic[8,11]. In the process of adsorption for CH_4 recovery in the coal bed, N_2 (N_2-ECBM) and CO_2 (CO_2-ECBM) molecules compete with CH_4 for adsorption sites, which forms the theoretical basis for methane recovery in the coal bed[14]. Therefore, it is important to gain a deep insight into the adsorbent structure and adsorption mechanism during the competitive adsorption process. Coal-derived asphaltenes, distinguished by their dense, active polyaromatic structure and distinctive characteristics, play a pivotal role in adsorbing gases in both the CO_2-Enhanced Coalbed Methane Recovery (CO_2-ECBM) and N_2-Enhanced Coalbed Methane Recovery (N_2-ECBM) processes. Notably, heteroatoms such as N, O, and S can be found within asphaltene molecules, contributing to their remarkable properties[15,16].

Recently, there has been a growing interest in applying computational methods such as MD, DFT, and GCMC to study and analyze competitive adsorption on asphaltene structures derived from coal[11,17]. In a previous study conducted by one of the authors[18], theoretical GCMC, MD, and DFT methods were employed to examine the impact of the pyrrole functional group in asphaltene derived from model coal on the selective adsorption of CO_2. These research findings indicate that the NH functional group enhances the selective adsorption of CO_2. In this study, we utilized the MD, DFT, and GCMC methods to investigate the competitive adsorption of CO_2, N_2, and CH_4 in the CO_2-ECBM and N_2-ECBM processes on a model asphaltene doped with CH_2, NH, O, and S atoms.

Method

Molecular model

For this research, we referred to the study conducted by Schuler et al. to select an asphaltene molecule[19]. Their work utilized both atomic force microscopy (AFM) and scanning tunneling microscopy (STM) to reliably identify asphaltenes, thereby establishing a robust foundation for structure identification. Therefore, we chose PA3 as the adsorbent. Molecular structures of the asphaltene model and adsorbate gases are shown in Fig. 1. According to reference articles[19,20], in position X (see Fig. 1), there can be a heteroatom such as CH_2, NH, or O. For the purpose of this study, we incorporated CH_2, NH, O, and S groups as heteroatoms into the asphaltene structure to assess the adsorption of CO_2, CH_4, and N_2.

Grand canonical Monte Carlo and molecular dynamics

An appropriate force field is crucial for molecular simulations to accurately represent atomic interactions and align with experimental outcomes. In our research on coal products, we evaluated various force fields, including Dreiding, CVFF, PCFF, and COMPASS, based on a literature review[21–23]. We compared the molecular densities of PA3 obtained from different force fields with the experimentally determined actual densities of coal products. The results, detailed in Fig. 2, indicate that the COMPASS force field closely approximates real values.

In addition, the COMPASS force field has a proven track record for simulating oil molecules and CO_2 adsorption[22,24]. Consequently, for all simulations, COMPASS was adopted as the force field, with a cutoff radius of 12.5 angstroms. Furthermore, we assessed the adsorption isotherms obtained through our simulations and experimental data[25], as presented in Fig. S1, to validate our methodology. Both datasets showed strong agreement with the Langmuir–Freundlich model.

Initially, we constructed a simulation container with 20 PA3 molecules (comprising five types: PA3C, PA3O, PA3N, and PA3S), in which the density was 1.2 g/cm^3. We utilized the SMART minimization algorithm to perform geometry optimization and obtain the initial configuration[26,27]. Using the Amorphous Cell module of the Materials Studio software, we generated coal-derived asphaltene. Subsequently, we conducted equilibration through annealing dynamics at various temperatures (300–1000 K), as illustrated in Fig. 3.

We utilized the GCMC technique with the Metropolis algorithm, employing the sorption module within Materials Studio, to investigate the selective adsorption of gases and establish the adsorption isotherms[28]. The temperature range of the simulations was 273–373 K, while the pressure was fixed (0–10000 kPa). The simulation parameters were chosen as 10^6 equilibration steps and 10^7 production steps. The van der Waals interactions were examined using the Lennard-Jones potential, while the electrostatic interactions were investigated using
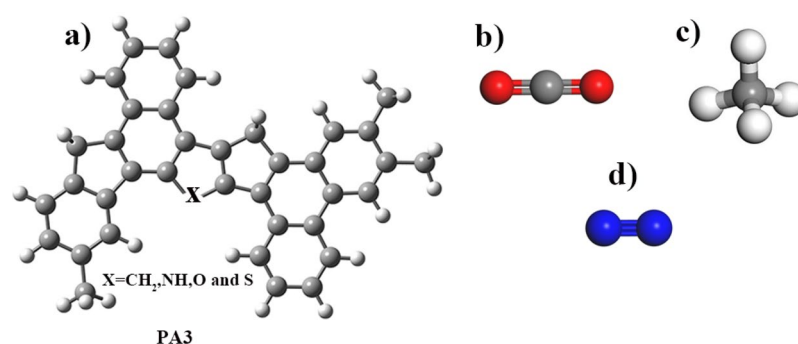

Figure 1. Molecular structures of (**a**) PA3, (**b**) CO_2, (**c**) CH_4, and (**d**) N_2.
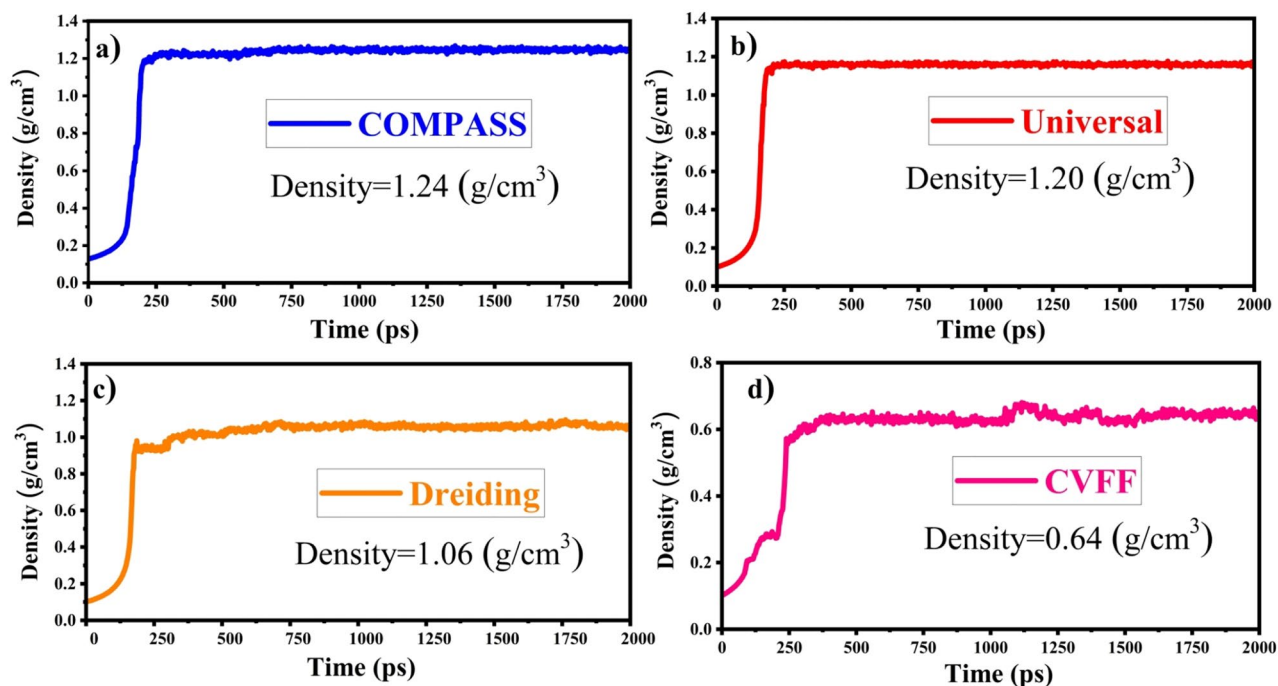
Figure 2. Density in the dynamics process. The NVT ensemble system was thermalized and equilibrated using 200 ps at 298 K. The NPT ensemble was used for 2 ns. The first 1 ns were used for relaxation, and the last 1 ns were used to calculate the density. The Nosé-Hoover thermostat and Berendsen barostat were used to control the temperature and pressure, respectively.
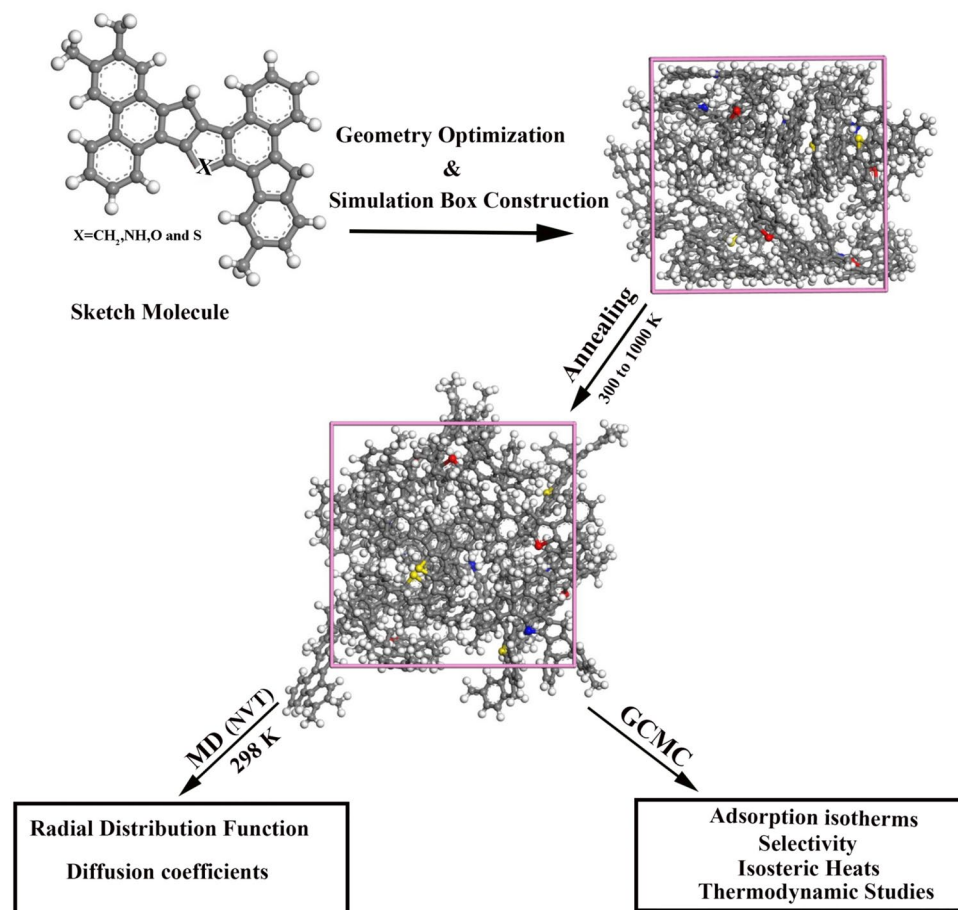

Figure 3. The process of molecular simulation for PA3.

the Coulombic term. For the MD simulations, the NVT ensemble with a Nose–Hoover temperature thermostat was used. The analysis focused on the final 0.4 ns of each MD simulation, which covered a total duration of 2 ns at 298 K, with a time step of 1 fs.

Density functional theory

In this study, we utilized DFT calculations to investigate the impact of substituting four heteroatoms with each other on the electronic properties of asphaltene molecules derived from coal. Our aim was to enhance our comprehension of the adsorption process of CH_4, N_2, and CO_2 molecules on asphaltene. DFT calculations were performed using Gaussian 09 software based on simulations from previous studies[29–31]. Analyzes such as theoretical reactivity parameters (hardness, chemical potential, and electrophilicity) and ESP maps were obtained using the B3LYP exchange-correlation functional and 6-311++G(d,p) basis set. We chose the B3LYP exchange-correlation functional for computing electronic parameters because of its accuracy and low computational cost. We optimized the PA3, gas molecules, and PA3-gas molecule complex with the ωB97XD exchange-correlation functional and 6-31+G(d,p) basis set. The adsorption energy was calculated using this level of theory. The reason we chose this exchange-correlation function was that it considers dispersion interactions due to its unique formalism[32,33]. We conducted a non-covalent interaction (NCI) analysis using the optimized adsorbent-adsorbate geometry at the ωB97XD/6-31+G(d,p) level of theory. Furthermore, we performed a non-covalent interaction (NCI) analysis using Multiwfn and VMD software.

Results and discussion
Monte Carlo in the grand canonical ensemble
Adsorption competition
Adsorption isotherms are essential tools for establishing a relationship between adsorption loading and different pressures at a constant temperature. This study focuses on examining the adsorption tendencies of CO_2, CH_4, and N_2 within a model coal-derived asphaltene using the GCMC method. This investigation was conducted across a temperature spectrum, including 273 K, 298 K, 323 K, and 348 K, while the pressure ranged from 0.0-10000 kPa. In the following, we introduce the models used to describe the adsorption process.

The Langmuir model[34] is based on the notion that adsorbate molecules adhere to the surface of an adsorbent to form a single molecular layer. This model assumes that the surface of the adsorbent features uniform binding sites[35]. The Langmuir model is represented by the following equation[34]:

$$q = \frac{abp}{1 + abp} \tag{1}$$

Parameter a signifies the monolayer adsorption capacity (mL/g), b corresponds to the adsorption equilibrium constant (kPa^{-1}), p is the pressure (kPa), and q represents the adsorption amount in units of (mL/g).

Furthermore, the Freundlich model was used to analyze the adsorption isotherms. This empirical isotherm was designed to represent multilayer (heterogeneous) adsorption. The mathematical representation of the Freundlich model is given by the following equation[34]:

$$q = kp^{\frac{1}{n}} \tag{2}$$

here, k is Freundlich constant ($mLg^{-1}kPa^{-\frac{1}{n}}$), and n characterizes the heterogeneity of the adsorbent. In the context of adsorption, an n value greater than one indicates that the adsorbate is more likely to bind to the adsorbent surface.

Although both previously described models find utility across various systems, their individual limitations have motivated the adoption of a combined approach. This is a result of the inherent shortcomings of both models[36]. The integration of these equations results in the Langmuir–Freundlich model, which effectively addresses the intrinsic heterogeneity of adsorbents. The following equation encapsulates this model[11]:

$$q = \frac{abp^{\frac{1}{n}}}{1 + bp^{\frac{1}{n}}} \tag{3}$$

The Langmuir–Freundlich model effectively represents numerous heterogeneous systems[37,38]. In this model, variables a and b demonstrate a significant inverse relationship with the temperature[11,39]. Parameter b quantifies the inclination of the gas to adhere to the surface of an adsorbent[40], whereas n indicates the heterogeneity of the adsorbent surface.

Figure 4 illustrates the changes in adsorption capacity in response to pressure variations for CO_2, CH_4, and N_2 at different temperatures based on the Langmuir–Freundlich isotherm (refer to Figs. S2, S3 for the Freundlich and Langmuir isotherms, respectively). The data indicate a clear increase in the adsorption capacity for each gas as the pressure increases. As expected, the adsorption capacities of all gases were negatively correlated with changes in temperature[40]. Furthermore, heterogeneous adsorption on the surface of PA3 is evident, as the adsorption rate decreases with increasing pressure. Initially, gas molecules preferentially occupy available sites, and as pressure increases, sites with varying energy levels become occupied. Based on this figure, the average load per cell at 273 K is as follows:

CO_2 (14.20) > CH_4 (10.20) > N_2 (7.60).

Clearly, the contrast in the adsorption quantity is more pronounced for CO_2 than for CH_4 and N_2. The reasons for these results are thoroughly explored in the Adsorption Energy Calculation section. Furthermore, Table 1 presents the relevant parameters and R^2 values for the gases, as determined by the Langmuir–Freundlich model.
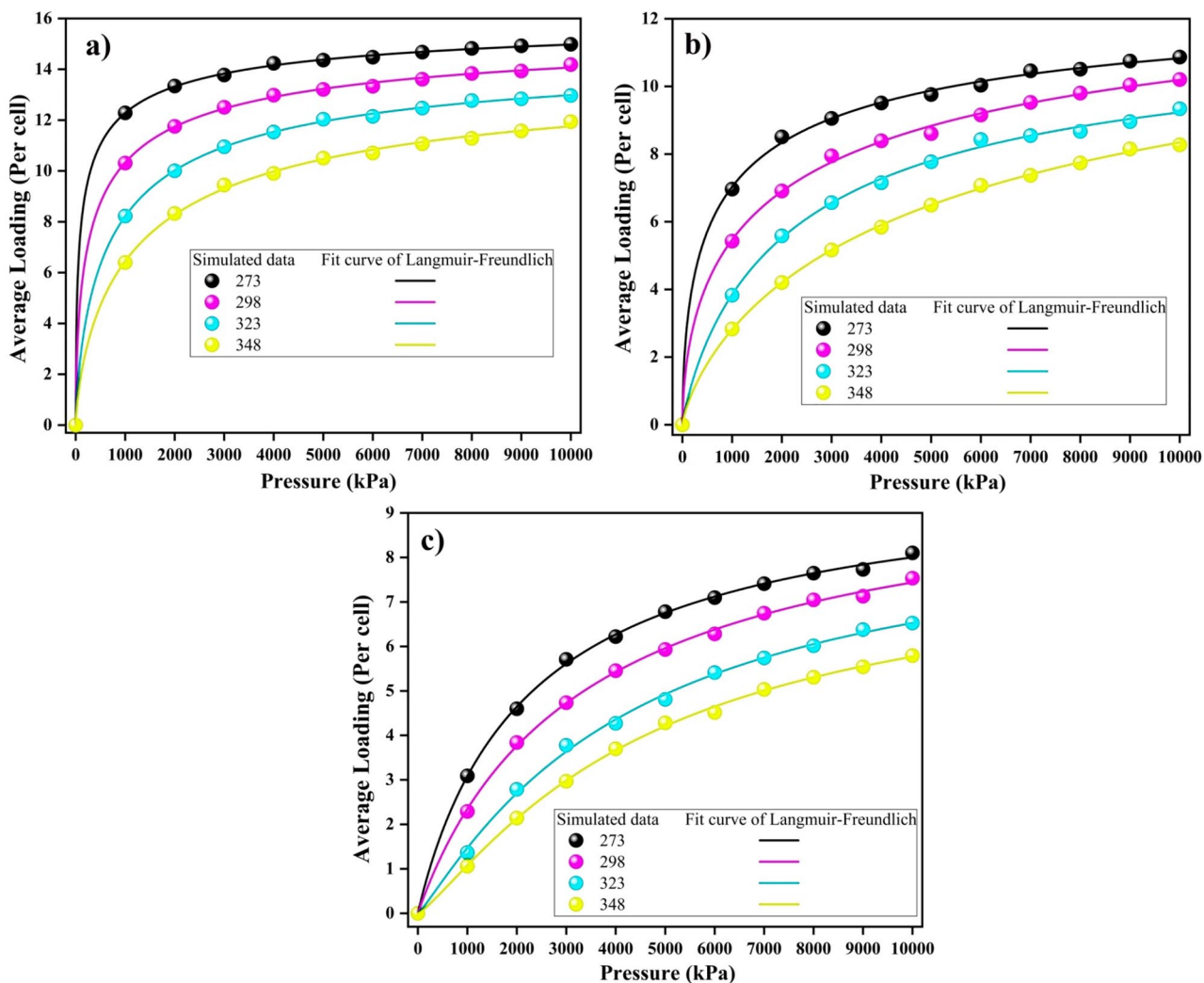
Figure 4. Langmuir–Freundlich isotherms for (**a**) CO_2, (**b**) CH_4, and (**c**) N_2 on model coal-derived asphaltene at various temperatures.

Adsorbent	T(K)	a (mL/g)	b (kPa^{-1})	n	R^{2*}
CO_2	273	16.53	0.0791	1.91	0.9998
	298	16.09	0.0302	1.70	0.9997
	323	14.93	0.0075	1.35	0.9998
	348	14.43	0.0056	1.36	0.9991
CH_4	273	13.55	0.0211	1.76	0.9992
	298	12.91	0.0162	1.52	0.9989
	323	11.93	0.0014	1.34	0.9986
	348	11.12	0.0010	1.35	0.9996
N_2	273	9.94	0.0058	1.905	0.9992
	298	9.45	0.0036	1.366	0.9991
	323	8.96	0.0034	1.256	0.9982
	348	8.06	0.0026	1.143	0.9986

Table 1. Langmuir–Freundlich model coefficients for adsorption isotherms of CO_2, CH_4, and N_2 on model coal-derived asphaltene at various temperatures. * Note: R^2: the nonlinear regression coefficient.

Additional findings derived from both the Langmuir and Freundlich models are presented in the Supporting Information, especially in Tables S2–S4. Remarkably, the model effectively encapsulated the adsorption patterns exhibited by all gases on the model coal-derived asphaltene, as indicated by the R^2 values.

Selectivity of adsorption
During adsorption, the selectivity parameter measures the relative affinity of an adsorbent for different adsorbates. We used it to assess the adsorption of CO_2, CH_4, and N_2 within PA3 in a competitive manner. The following equation defines the selectivity parameter[1]:

$$S = (\frac{x_{CO_2}}{x_b})/(\frac{y_{CO_2}}{y_b}), \qquad b = CH_4, CO_2 \text{ and } N_2 \tag{4}$$

here, x_i and y_i denote the proportion of the gas component i in the adsorbed and bulk phases, respectively. Considering the distinct adsorption strengths of gases onto PA3, we conducted simulations at five different temperatures with varying pressures to investigate selectivity, see Fig. 5. From the figure, PA3 shows a higher selectivity for CO_2 than for N_2 and CH_4 at all temperatures. Furthermore, the selectivity increased as the temperature rose, indicating a positive correlation. When it comes to pressure, it exhibits a negative correlation with selectivity. At a certain threshold of high pressure, it counteracts the impact of temperature, resulting in a consistent selectivity value across all temperatures. This phenomenon arises because at low pressures (corresponding to low adsorption loading), more active sites are available. As the loading increased, the number of active sites decreased. Consequently, additional gas molecules must adhere to and occupy less favorable sites, resulting in reduced selectivity as the pressure increases[41]. Overall, due to the elevated selectivity of PA3 for CO_2, demonstrates greater adsorption capabilities than CH_4 and N_2.

Isoteric heats
To delve deeper into the selective adsorption of gases, we introduce the concept of the isosteric heat of adsorption[1]. Given that adsorption is inherently an exothermic process, evaluating the quantified heat release can offer insights into binding strength[11]. The isosteric heat Q_{st} (Kcal/mol) was calculated using[14]:

$$Q_{st} = R_g T - \frac{\langle N_{ad} U_{ad} \rangle - \langle N_{ad} \rangle \langle U_{ad} \rangle}{\langle N_{ad}^2 \rangle - \langle N_{ad} \rangle^2} \tag{5}$$

where T (K) is the temperature, R_g (Kcal.mol^{-1}.K^{-1}) is the universal gas constant, U_{ad} (Kcal) represents the energy of adsorption, and N_{ad} (mol) denotes the total number of adsorbates.

The corresponding Q_{st} values for the adsorption of gases under varying pressure are illustrated in Fig. 6. Upon initial inspection of the plots, we observed a decrease in the isosteric heat with increasing temperature and pressure. The decrease in isosteric heat of adsorption with increasing temperature can be attributed to the exothermic nature of the process[42]. As the temperature increased, the thermal energy also increased, leading to a reduction in the energy gap between the adsorbed and non-adsorbed states. This weakens the binding strength, leading to lower isosteric heat. Moreover, isosteric heat is associated with the enthalpy change[43]. As the temperature increases, adsorption becomes less spontaneous, resulting in lower absolute values of the enthalpy change, and a decrease in isosteric heat.

The noticeable heat release observed at lower pressure levels may stem from the diverse energy levels of the active adsorption sites and the tendency of gas molecules to adhere to these sites, resulting in a significant
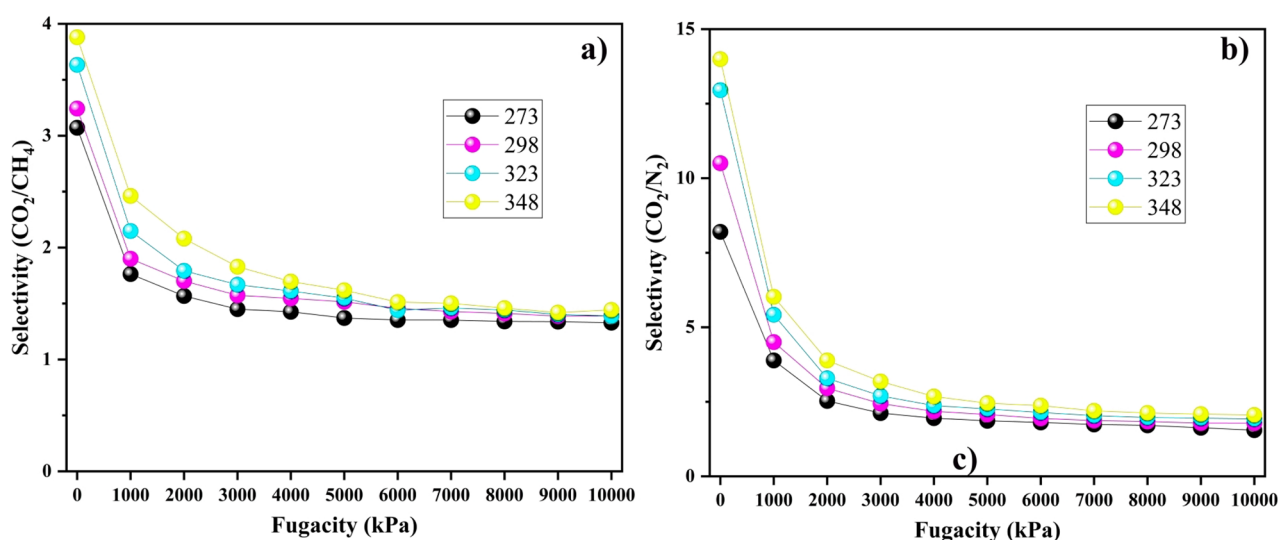

Figure 5. Selectivity of model coal-derived asphaltene for the adsorption of CO_2 over (**a**) CH_4 and (**b**) N_2 at different temperatures.
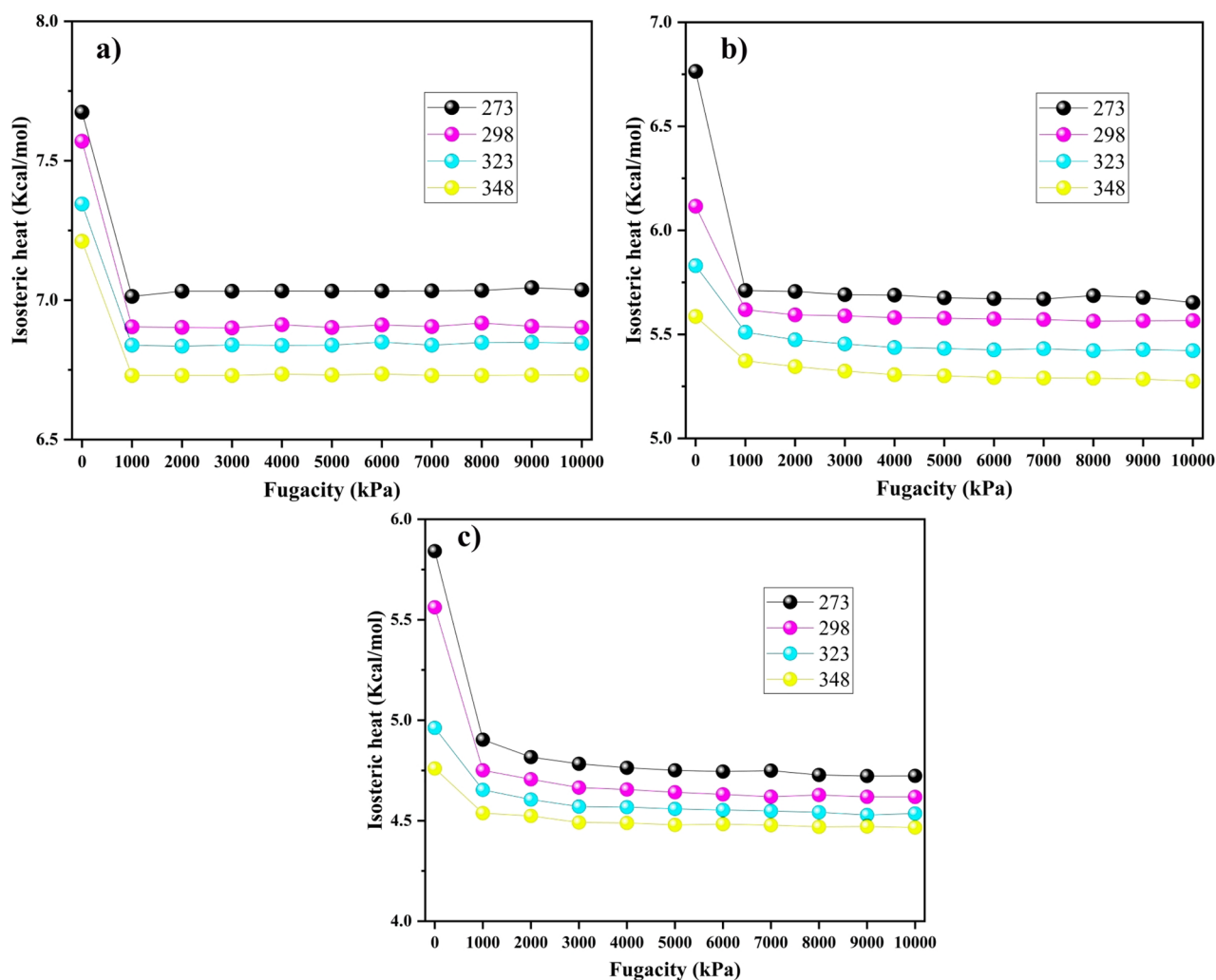
6

Figure 6. Isosteric heats of (**a**) CO_2, (**b**) CH_4, and (**c**) N_2 with varying adsorption pressure at different temperatures.

generation of heat[8]. Subsequently, in the range of 0-10 MPa, due to the decrease in favorable sites, the isosteric heat curves for all gases stabilized. It should be noted that CO_2 has a higher isosteric heat than CH_4 and N_2, while being less sensitive to temperature. Furthermore, all gases showed isosteric heat values below 10 kcal/mol for adsorption on PA3, indicating a physisorption process[44,45].

Assessment of adsorption affinities

To investigate the interaction of gases with the surface of the adsorbent, we utilized Henry's constant[46]. Henry's law describes a direct correlation between the amount of adsorption and the equilibrium pressure in the low-pressure regime. This relationship is expressed as follows[46]:

$$\frac{p}{q} = \frac{1}{K_H} exp(A_1 q + A_2 q^2 + A_3 q^3 + ...) \tag{6}$$

$$q = K_H p \tag{7}$$

In this equation, coefficients A_1, A_2, and A_3, along with Henry's coefficient K_H ($mLg^{-1}kPa^{-1}$), adsorption quantity q, and p representing the equilibrium pressure, play key roles. A higher K_H indicates a greater affinity between the adsorbate and adsorbent. K_H values for the gases in the adsorption process at different temperatures are illustrated in Fig. 7. It is evident that the temperature correlates negatively with K_H; higher temperatures and K_H significantly diminish the adsorption affinity of all gases. Compared to N_2 and CH_4, the Henry's constant for CO_2 exhibits a slightly greater sensitivity to temperature changes. The variation in K_H values for CO_2, CH_4, and N_2 reflects their effectiveness in the adsorption process. Notably, CO_2 exhibits a higher K_H value than the other gases. Furthermore, the polarizabilities of CO_2, CH_4, and N_2 are 29.1, 25.9, and 17.6, respectively[47,48]. Considering these values, the increased polarizability of CO_2 makes its interaction with the surface of PA3 more effective than that of the other gases.
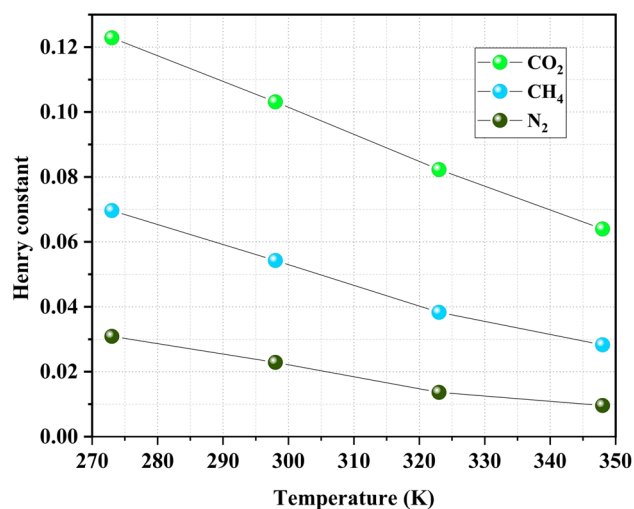
Figure 7. Henry constants of CO_2, CH_4, and N_2 in model coal-derived asphaltene at various temperatures.

Thermodynamic analysis

Due to the crucial role of thermodynamic studies in understanding adsorption behavior, we conducted an in-depth analysis to gain a comprehensive understanding.

Surface potential

The surface potential energy Ω (J/g) represents the energy required for the adsorbate to detach from the adsorbent surface. We computed this using the following equation[11]:

$$\Omega = -RT \int_0^p \frac{q}{p} dp \qquad (8)$$

The universal gas constant is represented by R, the absolute temperature is denoted by T, and the adsorption loading is indicated by q. Molecules with a higher absolute surface potential exhibit greater adsorption onto the adsorbent surface[46]. Because adsorption is a process that releases energy, Ω takes values below zero.

Plots of Ω with varying pressures for the adsorption of CO_2, CH_4, and N_2 on PA3 are depicted in Fig. 8. For each simulation, the absolute magnitudes of the surface potential for the gases increased under elevated pressures. This phenomenon may arise from the need for additional energy to accommodate adsorbates within the cavities of the porous material under high-pressure conditions[49]. Furthermore, an increase in the absolute Ω values was observed for all gases when the temperature decreased. This contributed to the enhanced adsorption of gases on the surfaces of the adsorbents. Notably, for the adsorption of CO_2, the Ω value exhibited a significant increase with a decrease in temperature compared to the values of other gases, highlighting CO_2's advantage in competitive adsorption on the surfaces of the adsorbents.

Gibbs free energy

The following formula was used to determine the change in Gibbs free energy ΔG (J/ml)[11]:

$$\Delta G = \frac{\Omega}{q} \qquad (9)$$

Following the principle of minimum energy, interfaces naturally tend to minimize their surface energy. For a solid interface, the minimization of surface energy occurs through the adsorption of other molecules onto its surface. This means that significant changes in the surface free energy result in pronounced adsorption loading[49]. The Gibbs Free Energy difference (ΔG) indicates whether the adsorption process occurred spontaneously.

As demonstrated in Fig. 9, an examination of the changes in Gibbs free energy during the adsorption process of CO_2, CH_4, and N_2 on the adsorbents indicates the thermodynamic spontaneity of these processes, as evidenced by their negative values. Despite the unfavorable effect of increasing the temperature on the adsorption process, the influence of pressure is favorable for enhancing the spontaneity of adsorption. This is due to the higher likelihood of gas molecules adhering to the surface of the adsorbent under high pressures[11]. Notably, for CO_2 gas, ΔG has significantly higher absolute values than those of other gases, highlighting a greater level of spontaneity in CO_2 compared to CH_4 and N_2.

Entropy

The entropy change (ΔS) is a valuable tool for understanding adsorption behavior, as it indicates the degree of system disorder[11]. Studying the changes in entropy concerning adsorption capacity provides valuable insights into the arrangement of molecules on the surface of the adsorbent. This analysis provides crucial information regarding the adsorption process[46]. The entropy change ΔS (J.mL^{-1}K^{-1}) is defined using the following formula[11]:
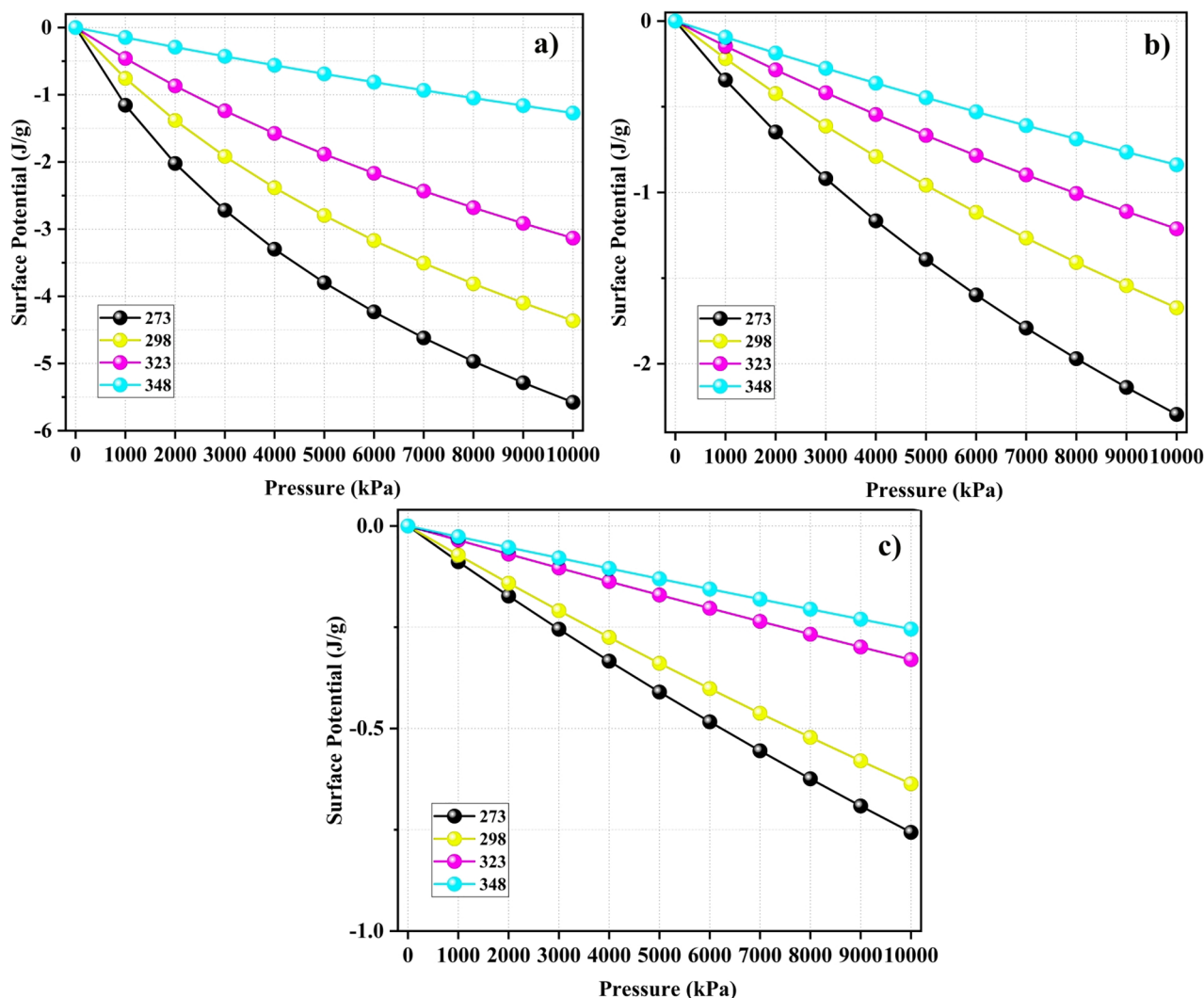
Figure 8. Surface potentials of (**a**) CO_2, (**b**) CH_4, and (**c**) N_2 in model coal-derived asphaltene at various temperatures.

$$\Delta S = \frac{\Delta H - \Delta G}{T} \tag{10}$$

T represents the absolute temperature and $\Delta H = -Q_{st}$[43]. Changes in entropy result from the interaction of different molecular movements, such as rotational degrees of freedom, vibrational modes, and the translational motion of gas molecules[46]. The ΔS values associated with gas adsorption on PA3 are depicted in Fig. 10. In general, the absolute magnitude of ΔS decreases with increasing pressure. At lower pressures, the gas molecules showed enhanced interactions with the surfaces of the adsorbents. This behavior arises because gas molecules, once adsorbed, can absorb additional energy from the environment and then detach from the adsorbent surface. If a gas exhibits a ΔS value below zero, it indicates a shift in the adsorption process. This shift progressed from disorder to order, resulting in an organized configuration of gas molecules on the surface of the adsorbent[11]. Remarkably, the most significant absolute change in entropy occurred during the adsorption of all gases at the lowest temperature (273 K) with increasing pressure. This suggests that the impact of the entropy change diminishes as the temperature increases.

Density functional theory
Theoretical reactivity parameters and molecular electrostatic potential
The difference in the electron energy levels between the highest occupied molecular orbital (HOMO) and lowest unoccupied molecular orbital (LUMO) can be considered a reliable indicator of changes in electronic properties and chemical reactivity. The reactivity parameters studied were the chemical potential μ (eV), electrophilicity ω (eV), and chemical hardness η (eV). Hardness is a parameter defined by the charge and polarizability of the system. It causes changes in the energy of the HOMO and LUMO, consequently altering the band gap. Chemical hardness is defined as an indicator of a molecule's resistance to charge transfer to the environment. This implies
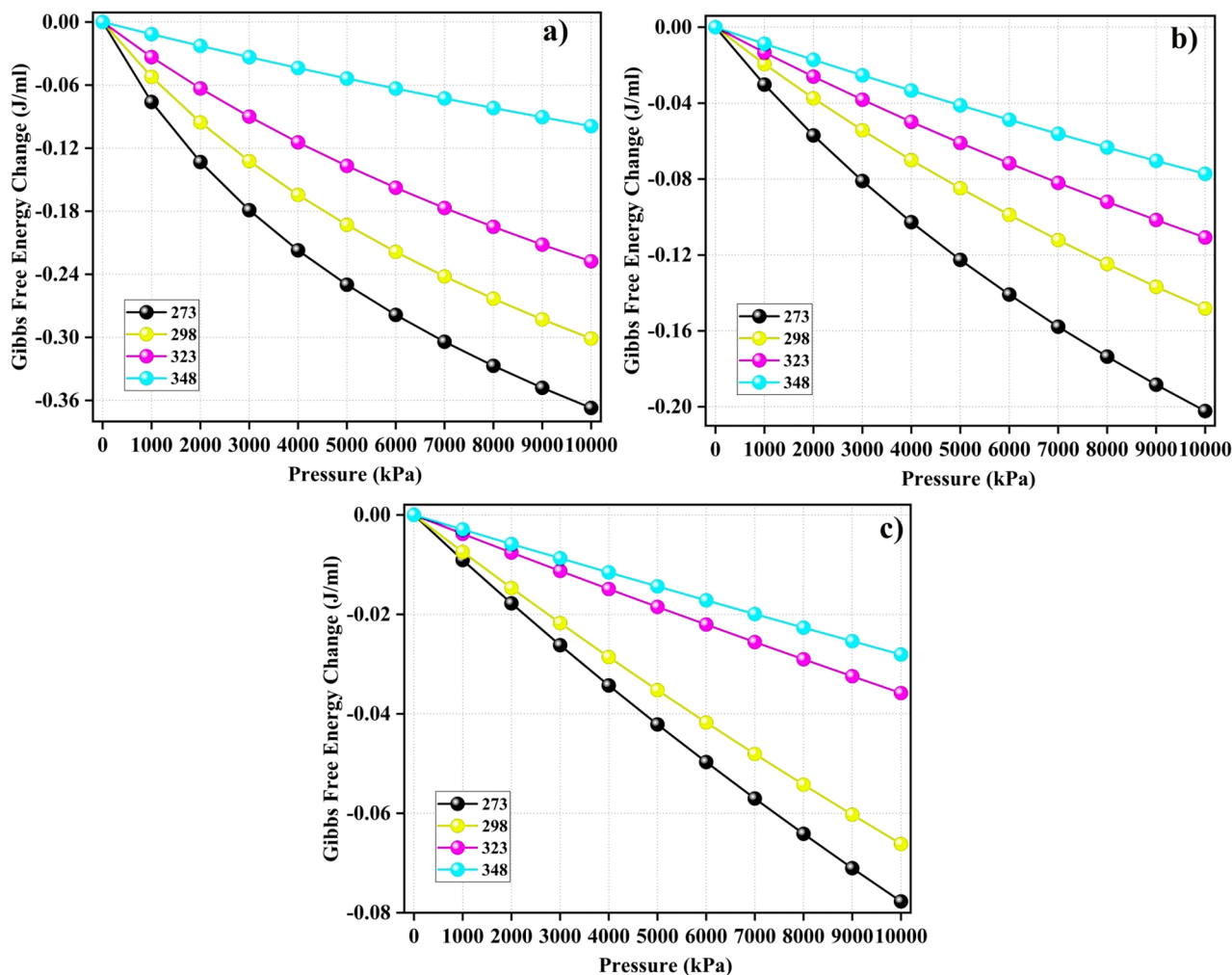
Figure 9. ΔG values associated with (**a**) CO_2, (**b**) CH_4, and (**c**) N_2 adsorption on the surface of model coal-derived asphaltene at various temperatures.

that the chemical hardness of a molecule has an inverse relationship with the charge transfer. The higher the chemical hardness of a molecule, the lower the chance of charge transfer and interaction of the molecule with its environment. The chemical potential is an indicator of the stability of the system and shows the tendency of the system to remain in its current conditions[50]. Koopman's theory calculates the chemical potential and hardness using the following equations[31]:

$$\eta = \frac{(IP - EA)}{2} = -\frac{1}{2}\left(E_{HOMO} - E_{LUMO}\right) \tag{11}$$

$$\mu = \frac{(IP + EA)}{2} = \frac{1}{2}\left(E_{HOMO} + E_{LUMO}\right) \tag{12}$$

IP (eV) refers to the ionization energy, which is equivalent to E_{HOMO} (eV), and EA (eV) represents the electron affinity. EA is proportional to $-E_{LUMO}$ (eV). Parr and his colleagues proposed a parameter called electrophilicity ω (eV), which determines whether a molecule is an electron acceptor or donor. Larger values of the electrophilicity parameter of the molecule indicate that the molecule is an electron acceptor. Electrophilicity can be defined as follows[51]:

$$\omega = \frac{\mu^2}{2\eta} \tag{13}$$

The values of the HOMO and LUMO orbital energies, band gaps, hardness, chemical potentials, and electrophilicity of functionalized PA3 calculated by the DFT B3LYP/6-311++G(d,p) level of theory are shown in Table 2. The chemical hardness values for the asphaltene structures follow the order:

PA3S > PA3O > PA3N > PA3C,

while the chemical potential values are as follows:
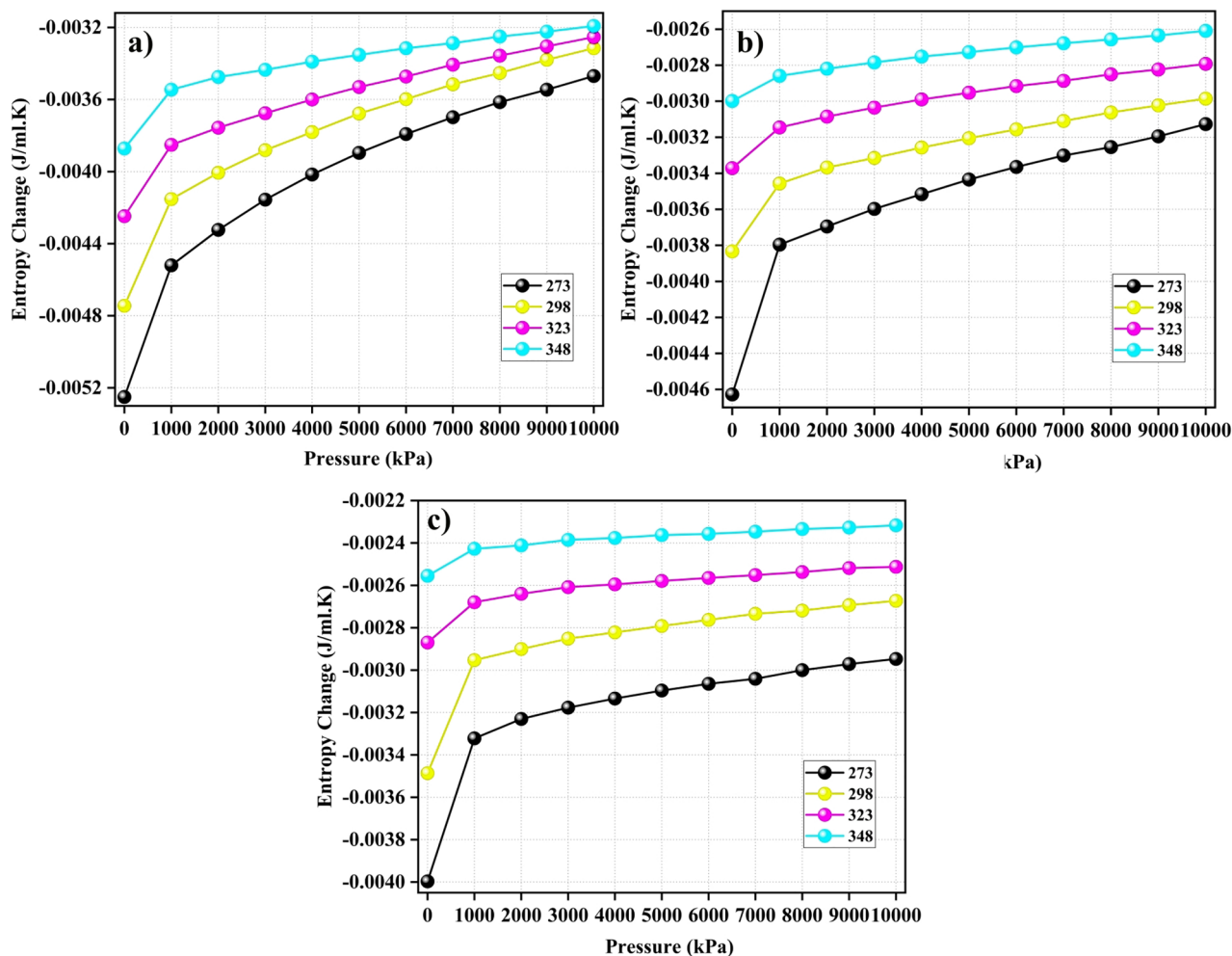
PA3N > PA3C > PA3O > PA3S.

Figure 10. Entropy changes during the adsorption of (**a**) CO_2, (**b**) CH_4, and (**c**) N_2 on model coal-derived at various temperatures.

Reactivity Parameters	PA3C	PA3S	PA3O	PA3N
E_{HOMO} (eV)	− 4.999	− 5.186	− 5.113	− 4.945
E_{LUMO} (eV)	− 1.813	− 1.853	− 1.789	− 1.672
$\Delta E_{HOMO-LUMO}$ (eV)	3.186	3.333	3.324	3.273
η (eV)	1.593	1.666	1.662	1.636
μ (eV)	− .401	− 3.521	− 3.451	− 3.308
ω (eV)	3.630	3.720	3.582	3.344
Dipole moment (Debye)	0.657	1.631	1.713	1.412

Table 2. The HOMO and LUMO orbital energies, band gap, hardness, chemical potential, and electrophilicity of functionalized PA3 were calculated using DFT at the B3LYP/6-311++G(d,p) level of theory.

These results indicate that the PA3S structure with the highest hardness also has the lowest chemical potential value. This suggests that the structure is stable and less likely to transfer charge or participate in reactions. The structures of PA3C and PA3N have the lowest hardness and the highest chemical potential, indicating their tendency to transfer charge. These findings are consistent with the adsorption energy data. The electrophilicity values follow the order:

PA3S > PA3C > PA3O > PA3N.

Molecular electrostatic potential analysis provides information about the active sites involved in the interaction between the adsorbent and the adsorbate. Color schemes often highlight these possibilities. In this map, as depicted in Fig. 11, the red color indicates high electron density values (nucleophilic sites), while the blue color indicates low electron density values (electrophilic sites). Therefore, by using ESP, it is possible to understand

which part of a molecule can participate more in interactions and, to some extent, help understand the reaction mechanism[52]. The 45.81 kcal/mol region on the PA3N molecule enhances its potential to interact with CO_2, N_2, and CH_4 compared to PA3C, PA3O, and PA3S.

When the methine group was used instead of a heteroatom in asphaltene, the electrostatic potential map showed that the methine group was electrophilic. This was reflected in the highly negative adsorption energies observed for the adsorption of gas molecules on their structure. Sulfur and oxygen atoms are nucleophilic as heteroatoms in the asphaltene structure; ESP plots for CO_2, CH_4, and N_2 are shown in Fig. S4. CO_2 adsorption on asphaltene structures has the highest (absolute) adsorption energy, which is attributed to the interaction between the highly electrophilic oxygen in CO_2 and the nucleophilic sites in the adsorbents. The structures of PA3N and PA3C have the lowest band gaps, indicating that these two structures are more reactive. This finding is consistent with the adsorption energy and chemical potential data.

Electron donors and acceptors were studied using electron density difference analysis. Here, we investigate the electron density differences to gain a better understanding of the interaction between the adsorbate and the surface. This difference is defined as follows[53]:

$$\Delta\rho(r) = \rho_{\text{Surf-Adsor}}(r) - \rho_{\text{Surf}}(r) - \rho_{\text{Adsor}}(r) \qquad (14)$$

$\rho_{\text{Surf-Adsor}}(r)$ denotes the electronic density of the surface covered by the adsorbate, while $\rho_{\text{Surf}}(r)$ and $\rho_{\text{Adsor}}(r)$ denote the densities of the surface and the adsorbate, respectively. This difference demonstrates the redistribution of the electronic density that occurs as a result of adsorption. The plots in Fig. S5 show that the adsorbates have a positive electron density difference, indicating that they are acceptors, while the asphaltenes are electron donors. The functional groups on the asphaltene structures (N, O, S) also have a positive electron density difference, indicating that they are acceptors. In contrast, the C group at the same position exhibits a negative electron density difference.

Adsorption energy calculation
The adsorption energy E_{ads} (KJ/mol) was calculated to further evaluate the adsorption mechanism of CO_2, CH_4, and N_2 gas molecules on asphaltene molecules derived from the model coal.
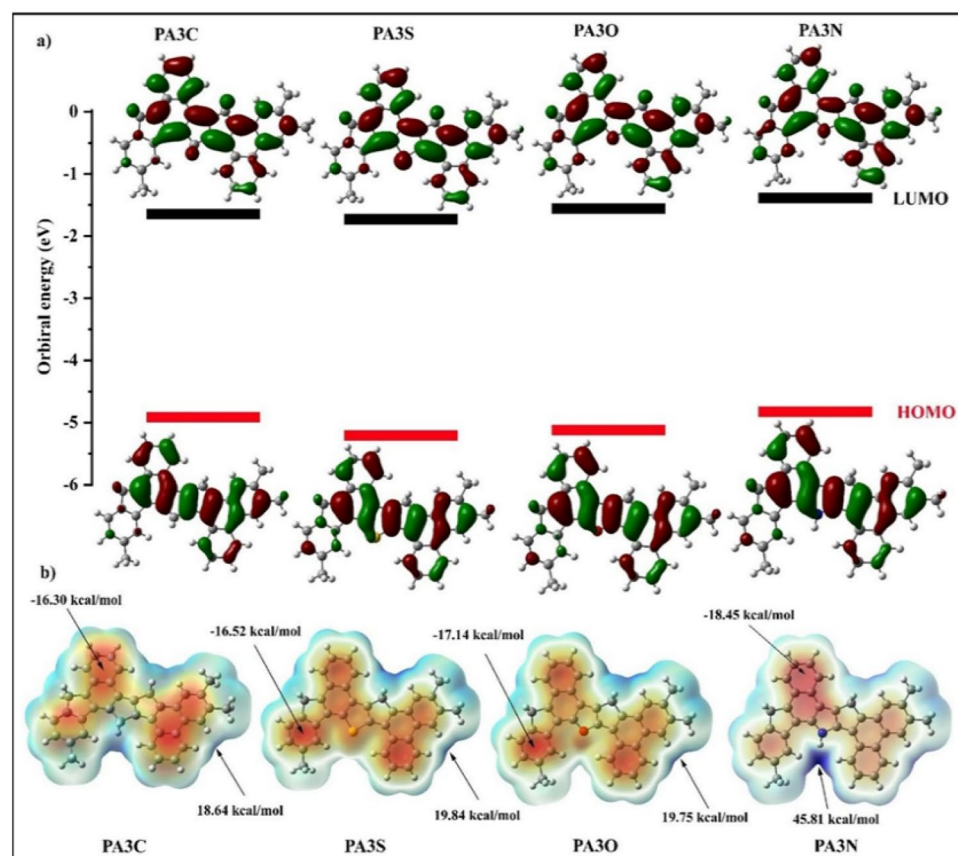

Figure 11. The diagram of HOMOs and LUMOs of functionalized PA3 using the B3LYP functional and the 6-311++G(d,p) basis set. Additionally, it includes molecular electrostatic potential (MEP) maps for the functionalized asphaltene (PA3) molecule, indicating regions of maximum (red) and minimum (blue) electron density.

$$E_{ads} = E_{a+s} - E_s - E_a, \tag{15}$$

where E_a represents the energy of the adsorbates, E_s is the energy of functionalized PA3, and E_{ads} represents the energy of the adsorbate-functionalized PA3 structure complex. Figure 12 shows the optimized structures of molecule adsorption on carbon oxide on the four asphaltene structures, along with their adsorption energies. Other structures are shown in Figs. S6, S7. Additionally, Table S5, displaying all adsorption energies, is included. For the adsorption of CO_2 and N_2 molecules, the adsorption energy values follow the order:

PA3N < PA3C < PA3O < PA3S.

For the adsorption of CH_4 on coal-derived asphaltenes, the adsorption energy values follow the order:

PA3N < PA3O < PA3S < PA3C.

The adsorption energy values indicate the physical adsorption of gas molecules onto all the asphaltene structures investigated in this study. Figure 13 illustrates an analysis of the adsorption energies (E_{ads}) of CO_2, CH_4, and N_2 on the PA3 surface. The highest (absolute) adsorption energy belongs to the adsorption of CO_2 on PA3N due to the $\pi - \pi$ interaction between CO_2 and the aromatic rings of asphaltene, as well as van der Waals interactions between the adsorbate and adsorbent. The adsorption energy for the adsorbates follows the order $N_2 > CH_4 > CO_2$. Furthermore, other adsorbent-adsorbate structures also exhibit $\pi - \pi$ interactions, while hydrogen bonding is less commonly observed. The adsorption energies were calculated at the ωB97XD/6-31+G(d,p) level of theory.

Nature of interactions

Non-covalent interactions are utilized to comprehend the nature of intermolecular forces between molecules. The NCI relies on the electron density and reduced density gradient (s), as shown in the following equation[54,55]:

$$s = \frac{1}{2(3\pi^2)^{1/3}} \frac{\nabla \rho}{\rho^{\frac{4}{3}}} \tag{16}$$

This analysis can be used to determine intermolecular forces, such as hydrogen bonding, van der Waals interactions, and repulsive steric interactions. Two general methods were used for this analysis. In the first method, a graph is generated with plots of the reduced density gradient (s) versus (sign $\lambda_2)\rho$, where (sign $\lambda_2)\rho$ represents
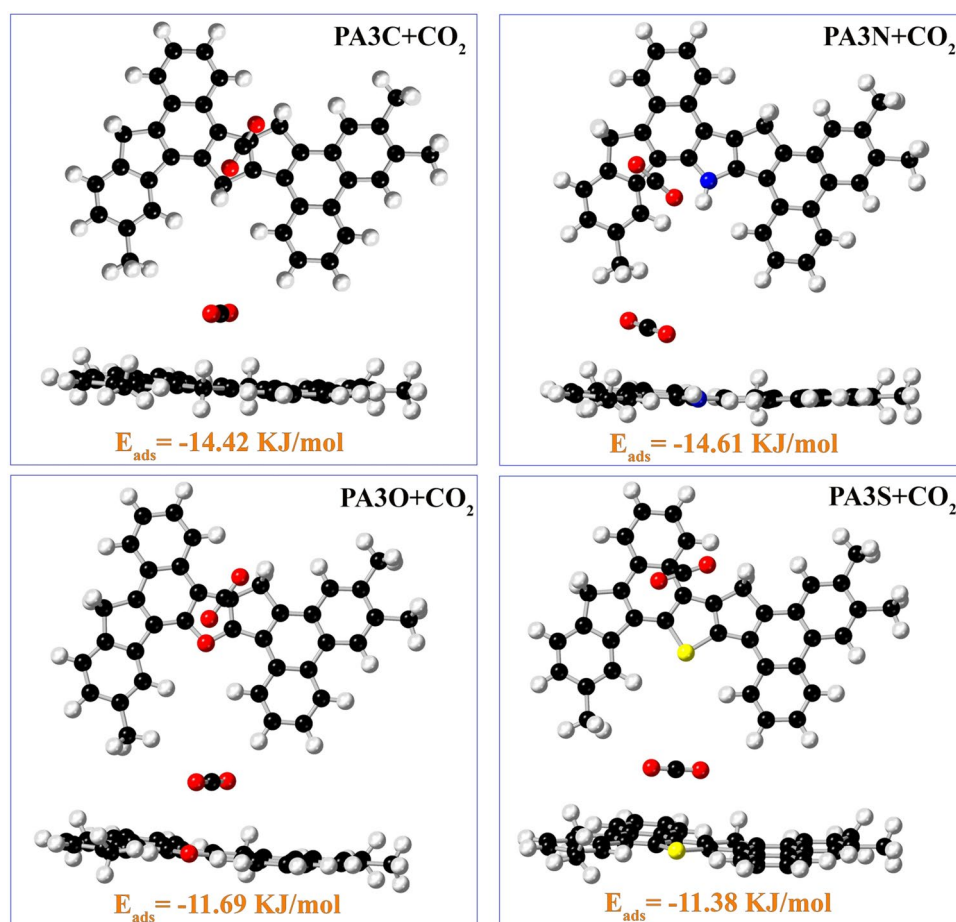

Figure 12. Stable adsorption configurations of the CO_2 molecule adsorbed on the surface of asphaltene fragments.
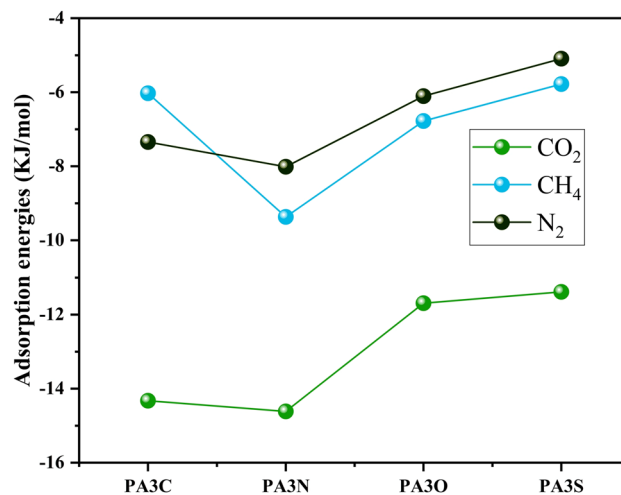
Figure 13. Examination of adsorption energies (E_{ads}) of CO_2, CH_4, and N_2 by the surface of asphaltene fragments.

the electron density multiplied by the sign of the second Hessian eigenvalue (λ_2). The value of (sign λ_2)ρ is useful for predicting the nature of the interaction. RDG and sign (λ_2) (r)ρ(r) define specific areas. Based on (λ_2) and (ρ), sign(λ_2)ρ < 0 indicates hydrogen bonding here, sign(λ_2)ρ > 0 indicates a repulsive interaction, and sign(λ_2)ρ $\approx$ 0 implies van der Waals interactions[54]. In the second method, intermolecular interactions in the NCI method can be visualized by using the gradient isosurface in the real space of the molecules. In the 3D visualization of NCI isosurfaces, green represents van der Waals interactions, blue indicates hydrogen bonding, and red signifies repulsive steric interactions[55,56]. To investigate intermolecular interactions, we utilized two- and three-dimensional non-covalent interaction analyses. The analysis of non-covalent interactions in three dimensions shows the van der Waals interactions (green color) for the adsorption of gas molecules on asphaltene structures. Figure 14 illustrates the reduced density gradient isosurfaces representing non-covalent interaction (NCI) regions during the adsorption of CO_2 on PA3C, PA3S, PA3N, and PA3O at the ωB97XD/6-31+G(d,p) level of theory. The isosurfaces were constructed with an RDG value of 0.6 au. With a color scaling range of -0.05 < (sign λ_2)ρ < 0.05 au. Other non-covalent interaction structures are depicted in the Supplementary Information. NCI analysis of the adsorption of CH_4 and N_2 on coal-derived asphaltenes is depicted in Figs. S8, S9. NCI analysis in two dimensions for the adsorption of CH_4, CO_2, and N_2 on the PA3C, PA3S, PA3N, and PA3O surfaces indicates van der Waals interactions (Fig. S10). According to the adsorption energies and optimized structures obtained from DFT calculations, we observed that the adsorption is physical in nature, indicating the absence of covalent interactions (chemical adsorption) between the adsorbates and adsorbents. Overall, the analysis of non-covalent interactions suggests physical interactions such as hydrogen bonding, van der Waals forces, and steric repulsion.

Molecular dynamics

Displacement analysis

Assessing the adsorption process requires a comprehensive understanding of the dynamic interactions between a gas and a solid sorbent. Self-diffusion coefficients provide valuable insights to assist in this process[14]. We used Einstein's method to calculate the self-diffusion coefficients D_S (cm^{-2}.s^{-1}) of gases within the nanopores of PA3. This method is expressed as follows[25]:

$$D_S = \frac{1}{6}\frac{d}{dt}\sum_{i=1}^{n}\langle|\mathbf{r}_i(t) - \mathbf{r}_i(0)|^2\rangle \tag{17}$$

here, $|\mathbf{r}_i(t) - \mathbf{r}_i(0)|^2$ represents the mean square displacement (MSD) of particles over time, and the angular brackets denote the ensemble average. A factor of 1/6 arises from the three-dimensional space, where each dimension contributes to the overall diffusion[8]. The self-diffusion coefficients at temperatures of 273 K, 298 K, 323 K, and 348 K for CO_2, CH_4, and N_2 within the model asphaltene are graphically illustrated in Fig. 15. It is evident that CO_2 has a significantly lower self-diffusion coefficient compared to the other two gases. The lower value of Ds for CO_2 confirms its stronger adsorption onto the model asphaltenes, indicating that CO_2 molecules exhibit more potent adsorption interactions than other gases.

Radial distribution function

Radial Distribution Function (RDF), a widely employed and effective technique, serves as a valuable tool for exploring interactions within molecular systems[57]. In particular, this method explores the potential existence of a specific chemical species (α) that may be present near another chemical group (β) separated by a defined distance (r). A representation of the RDF is outlined below[31]:
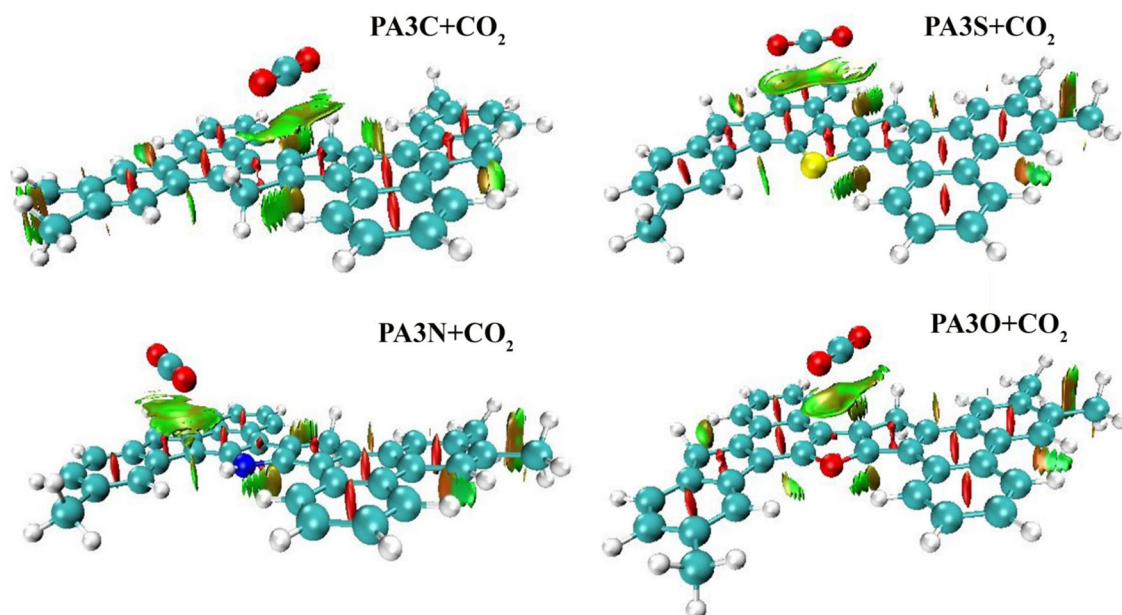
Figure 14. Three-dimensional representation of the analysis of non-covalent interactions (NCI) for CO_2 adsorption on PA3C, PA3S, PA3N, and PA3O at the 6-31+G(d,p) level of theory, illustrating van der Waals interactions. Diagrams were created using isosurfaces with RDG 0.6 au. The colors are marked from -0.05 < (sign λ_2)ρ < 0.05 au.

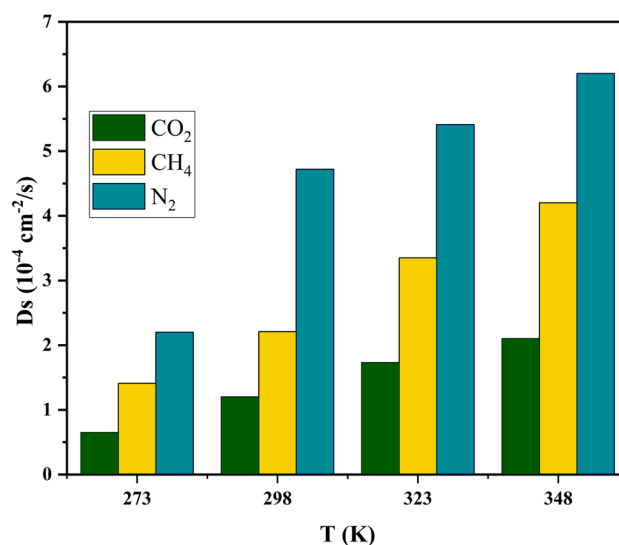**Figure 15.** Self-diffusion coefficients of CO_2, CH_4, and N_2 for adsorption onto the model coal-derived asphaltene as a function of temperature T = 273 K, 298 K, 323 K, and 348 K.

$$g_{\alpha\beta}(r) = \frac{V}{N_\alpha N_\beta}\left(\sum_{i=1}^{N_\alpha} \frac{n_i\beta(r)}{4\pi r^2 \Delta r}\right) \tag{18}$$

The provided formula includes various variables: V ($Å^3$) represents the volume of the system, N_α and N_β denote the numbers of particles α and β respectively, and the notation $n_i\beta(r)$ signifies the aggregated count of particles belonging to type β within a spherical shell located at a distance r (Å) from a particle of type α. Within the context of adsorption, RDF represents the ratio of density in a confined region to the average density of the entire system. This provides insight into the structure of the adsorption sites, especially for CO_2 adsorption on asphaltene molecules[1,8].

Figure 16 illustrates the RDF plots of the interactions between CO_2 and the PA3 surface. These interactions represent the following pairs: O-HN (O from CO_2 and H from PA3N), O-N (O from CO_2 and N from PA3N), O-C (O from CO_2 and C from all PA3 molecules), O-O (O from CO_2 and O from PA3O), and O-S (O from
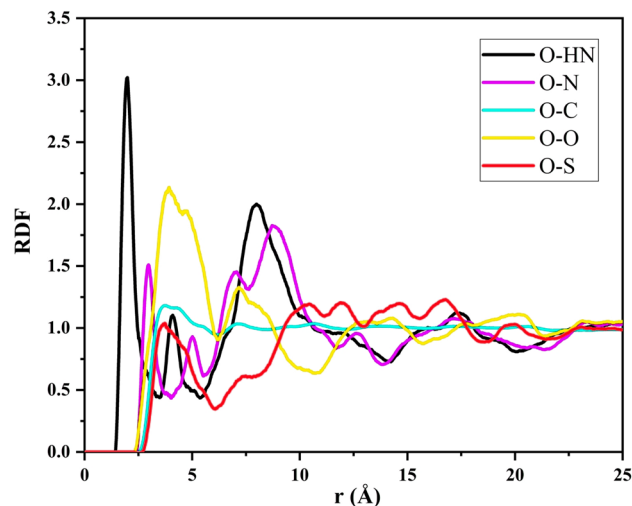
Figure 16. RDF between CO_2 and the PA3 surface with the following interactions: O-HN (O from CO_2 and H from PA3N), O-N (O from CO_2 and N from PA3N), O-C (O from CO_2 and C from all PA3 molecules), O-O (O from CO_2 and O from PA3O), O-S (O from CO_2 and S from PA3S).

CO_2 and S from PA3S). The RDF analysis revealed significant interactions, notably between the oxygens of CO_2 molecules and hydrogen atoms attached to the nitrogen in PA3N, as evidenced by a prominent peak at 2 Å. Additionally, noteworthy peaks were observed for the nitrogen in PA3-N, oxygen in PA3-O, and sulfur in PA3-S. These findings collectively emphasize the significant contributions of CO_2 oxygen atoms to the adsorption process of the model asphaltenes.

Conclusion

In this study, we employed grand canonical Monte Carlo, molecular dynamics, and density functional theory to analyze the adsorption behavior of CH_4, CO_2, and N_2 gases on a model asphaltene. We aimed to understand the mechanisms underlying competitive adsorption at various temperatures and pressures. We made several specific findings. It was found that an increase in temperature resulted in reduced adsorption, whereas an increase in pressure had a positive effect. Competitive adsorption favors CO_2 over CH_4 and N_2, especially at elevated temperatures. The adsorption of all gases exhibited isosteric heat values below 10 kcal/mol, indicating a physisorption process. CO_2 exhibits an advantage over the other two gases, as confirmed by the higher absolute values of the surface potential. All the adsorption processes were thermodynamically spontaneous, with CO_2 having the highest (absolute) Gibbs free energy. Entropy changes reflect the transition to an ordered phase during the adsorption process. The self-diffusion coefficients were the lowest for CO_2, indicating stronger interactions with the adsorbate. The DFT results indicate that the adsorption of CO_2 on asphaltenes derived from coal exhibited the highest (absolute) adsorption energies. Additionally, the adsorbent PA3N was found to be the most suitable for CO_2-ECBM and N_2-ECBM. Analysis of non-covalent interactions revealed that the primary interactions between the coal-derived asphaltenes and the CO_2, N_2, and CH_4 adsorbates are van der Waals forces. These findings highlight the complexity and significance of adsorption processes. Our findings provide a comprehensive understanding of the adsorption behavior of these gases, which could serve as a foundation for future research in this field. The insights gained from this study could be particularly useful for researchers investigating the adsorption properties of other gases and materials.

Data availability

The data will be available from the corresponding author upon a reasonable request.

References

1. Zhang, Y., Zhuo, J., Wu, Y. & Yao, Q. Molecular simulation of the adsorption behaviors of co2/ch4 in curvature, planar, and mixture models. *Energy Fuels* **34**, 4153–4161 (2020).
2. Grubb, M., Vrolijk, C. & Brack, D. *Routledge Revivals: Kyoto Protocol (1999): A Guide and Assessment* (Routledge, 2018).
3. Chen, S. *et al.* Using 13x, lix, and lipdagx zeolites for co2 capture from post-combustion flue gas. *Appl. Energy* **191**, 87–98 (2017).
4. Giraldo, L. J., Medina, O. E., Ortiz-Perez, V., Franco, C. A. & Cortès, F. B. Enhanced carbon storage process from flue gas streams using rice husk silica nanoparticles: An approach in shallow coal bed methane reservoirs. *Energy Fuels* **37**, 2945–2959 (2023).
5. Tambaria, T. N., Sugai, Y. & Nguele, R. Adsorption factors in enhanced coal bed methane recovery: A review. *Gases* **2**, 1–21 (2022).
6. Li, C., Yang, Z., Chen, J. & Sun, H. Prediction of critical desorption pressure of coalbed methane in multi-coal seams reservoir of medium and high coal rank: A case study of eastern yunnan and western guizhou, china. *Nat. Resour. Res.* **31**, 1443–1461 (2022).
7. Wen, G., Sun, H., Li, R., Fu, J. & Zhao, X. Assessment method and application of coalbed methane resources in coal mining stability area. *J. China Coal Soc.* **43**, 160–167 (2018).
8. Long, H. *et al.* Adsorption and diffusion characteristics of ch4, co2, and n2 in micropores and mesopores of bituminous coal: Molecular dynamics. *Fuel* **292**, 120268 (2021).

9. Sun, Y. *et al.* Characterisation and evolution of the full size range of pores and fractures in rocks under freeze-thaw conditions using nuclear magnetic resonance and three-dimensional x-ray microscopy. *Eng. Geol.* **271**, 105616 (2020).

10. Yang, W., Lu, C., Si, G., Lin, B. & Jiao, X. Coal and gas outburst control using uniform hydraulic fracturing by destress blasting and water-driven gas release. *J. Nat. Gas Sci. Eng.* **79**, 103360 (2020).

11. Hao, M., Qiao, Z., Zhang, H., Wang, Y. & Li, Y. Thermodynamic analysis of ch4/co2/n2 adsorption on anthracite coal: investigated by molecular simulation. *Energy Fuels* **35**, 4246–4257 (2021).

12. Baek, S. & Akkutlu, I. Y. Enhanced recovery of nanoconfined oil in tight rocks using lean gas (c2h6 and co2) injection. *SPE J.* **26**, 2018–2037 (2021).

13. Yin, T. *et al.* Application of molecular simulation in coalbed methane reservoirs: A systematic review. *Unconv. Resour.* **2**, 124–132 (2022).

14. Sun, H. *et al.* Competitive adsorption of co2 over n2 in asphaltene slit nanopores studied by molecular simulation. *Energy Fuels* **31**, 13979–13984 (2017).

15. Hu, Y., Wang, S. & He, Y. Investigation of the coal oxidation effect on competitive adsorption characteristics of co2/ch4. *Energy Fuels* **34**, 12860–12869 (2020).

16. Schuler, B. *et al.* Overview of asphaltene nanostructures and thermodynamic applications. *Energy Fuels* **34**, 15082–15105 (2020).

17. Tehrani, N. H. M. H. *et al.* Novel asphaltene-derived nanoporous carbon with ns-rich micro-mesoporous structure for superior gas adsorption: Experimental and dft study. *Chem. Eng. J.* **358**, 1126–1138 (2019).

18. Ekramipooya, A., Valadi, F. M., Latifipour, M., Rashtchian, D. & Gholami, M. R. Effect of the pyrrolic nitrogen functional group in the selective adsorption of co2: Gcmc, md, and dft studies. *Energy Fuels* **35**, 15918–15934 (2021).

19. Schuler, B., Meyer, G., Peña, D., Mullins, O. C. & Gross, L. Unraveling the molecular structures of asphaltenes by atomic force microscopy. *J. Am. Chem. Soc.* **137**, 9870–9876 (2015).

20. Ramírez, L., Moncayo-Riascos, I., Cortés, F. B., Franco, C. A. & Ribadeneira, R. Molecular dynamics study of the aggregation behavior of polycyclic aromatic hydrocarbon molecules in n-heptane-toluene mixtures: assessing the heteroatom content effect. *Energy Fuels* **35**, 3119–3129 (2021).

21. Sun, H. Compass: an ab initio force-field optimized for condensed-phase applications overview with details on alkane and benzene compounds. *J. Phys. Chem. B* **102**, 7338–7364 (1998).

22. Hu, H., Li, X., Fang, Z., Wei, N. & Li, Q. Small-molecule gas sorption and diffusion in coal: Molecular simulation. *Energy* **35**, 2939–2944 (2010).

23. Rogel, E. & Carbognani, L. Density estimation of asphaltenes using molecular dynamics simulations. *Energy Fuels* **17**, 378–386 (2003).

24. You, J. *et al.* Adsorption behavior of carbon dioxide and methane in bituminous coal: A molecular simulation study. *Chin. J. Chem. Eng.* **24**, 1275–1282 (2016).

25. Yu, S., Bo, J. & Meijun, Q. Molecular dynamic simulation of self-and transport diffusion for co2/ch4/n2 in low-rank coal vitrinite. *Energy Fuels* **32**, 3085–3096 (2018).

26. Khaled, K. *et al.* Alanine as corrosion inhibitor for iron in acid medium: A molecular level study. *Int. J. Electrochem. Sci* **7**, 12706–12719 (2012).

27. Khaled, K. & Al-Mhyawi, S. R. Electrochemical and density function theory investigations of l-arginine as corrosion inhibitor for steel in 3.5% nacl. *Int. J. Electrochem. Sci.* **8**, 4055–4072 (2013).

28. Frenkel, D. & Smit, B. *Understanding Molecular Simulation: From Algorithms to Applications* (Elsevier, 2023).

29. Ekramipooya, A., Valadi, F. M., Farisabadi, A. & Gholami, M. R. Effect of the heteroatom presence in different positions of the model asphaltene structure on the self-aggregation: Md and dft study. *J. Mol. Liq.* **334**, 116109 (2021).

30. Valadi, F. M., Ekramipooya, A. & Gholami, M. R. Selective separation of congo red from a mixture of anionic and cationic dyes using magnetic-mof: Experimental and dft study. *J. Mol. Liq.* **318**, 114051 (2020).

31. Abdollahizad, G., Valadi, F. M., Akbarzadeh, E. & Gholami, M. R. Adsorption properties of halloysite modified acrylamide/quince seeds-based hydrogel: Experimental and dft investigation. *J. Polym. Environ.* **30**, 4637–4650 (2022).

32. Chai, J.-D. & Head-Gordon, M. Systematic optimization of long-range corrected hybrid density functionals. *J. Chem. Phys.* **128**, 084106 (2008).

33. Chai, J.-D. & Head-Gordon, M. Long-range corrected hybrid density functionals with damped atom-atom dispersion corrections. *Phys. Chem. Chem. Phys.* **10**, 6615–6620 (2008).

34. Langmuir, I. The adsorption of gases on plane surfaces of glass, mica and platinum. *J. Am. Chem. Soc.* **40**, 1361–1403 (1918).

35. Kecili, R. & Hussain, C. M. Mechanism of adsorption on nanomaterials. In *Nanomaterials in Chromatography* 89–115 (Elsevier, 2018).

36. Li, J., Li, B., Ren, C., Zhang, Y. & Wang, B. An adsorption model for evaluating methane adsorption capacity in shale under various pressures and moisture. *J. Nat. Gas Sci. Eng.* **81**, 103426 (2020).

37. Charmas, B. & Leboda, R. Effect of surface heterogeneity on adsorption on solid surfaces: Application of inverse gas chromatography in the studies of energetic heterogeneity of adsorbents. *J. Chromatogr. A* **886**, 133–152 (2000).

38. Bagherinia, M. A. & Shadman, M. Investigations of co2, ch4 and n2 physisorption in single-walled silicon carbon nanotubes using gcmc simulation. *Int. Nano Lett.* **4**, 95 (2014).

39. Zhou, D., Feng, Z.-C., Zhao, D., Zhao, Y.-S. & Cai, T.-T. Experimental meso scale study on the distribution and evolution of methane adsorption in coal. *Appl. Thermal Eng.* **112**, 942–951 (2017).

40. Yan, M. *et al.* Factors influencing the gas adsorption thermodynamic characteristics of low-rank coal. *Fuel* **248**, 117–126 (2019).

41. Zhuo, S. *et al.* Computer simulation for adsorption of co 2, n 2 and flue gas in a mimetic mcm-41. *J. Phys. Chem. C* **112**, 11295–11300 (2008).

42. Tang, X., Wang, Z., Ripepi, N., Kang, B. & Yue, G. Adsorption affinity of different types of coal: mean isosteric heat of adsorption. *Energy Fuels* **29**, 3609–3615 (2015).

43. Duan, S., Gu, M., Du, X. & Xian, X. Adsorption equilibrium of co2 and ch4 and their mixture on sichuan basin shale. *Energy Fuels* **30**, 2248–2256 (2016).

44. Gao, D., Hong, L., Wang, J. & Zheng, D. Molecular simulation of gas adsorption characteristics and diffusion in micropores of lignite. *Fuel* **269**, 117443 (2020).

45. Ding, Y. & Alpay, E. Equilibria and kinetics of co2 adsorption on hydrotalcite adsorbent. *Chem. Eng. Sci.* **55**, 3461–3474 (2000).

46. Du, X. *et al.* Adsorption equilibrium and thermodynamic analysis of co2 and ch4 on qinshui basin anthracite. *Geofluids* **2019**, 1–14 (2019).

47. Du, X. *et al.* Thermodynamics analysis of the adsorption of ch4 and co2 on montmorillonite. *Appl. Clay Sci.* **192**, 105631 (2020).

48. Rallapalli, P. *et al.* Sorption studies of co 2, ch 4, n 2, co, o 2 and ar on nanoporous aluminum terephthalate [mil-53 (al)]. *J. Porous Mater.* **18**, 205–210 (2011).

49. Du, X. *et al.* Co2 and ch4 adsorption on different rank coals: A thermodynamics study of surface potential, gibbs free energy change and entropy loss. *Fuel* **283**, 118886 (2021).

50. Parr, R. G. & Pearson, R. G. Absolute hardness: Companion parameter to absolute electronegativity. *J. Am. Chem. Soc.* **105**, 7512–7516 (1983).

51. Parr, R. G., Donnelly, R. A., Levy, M. & Palke, W. E. Electronegativity: The density functional viewpoint. *J. Chem. Phys.* **68**, 3801–3807 (1978).

52. Akhtari, K. *et al.* A density functional theory study of the reactivity descriptors and antioxidant behavior of crocin. *Comput. Theor. Chem.* **1013**, 123–129 (2013).
53. Prates Ramalho, J., Dordio, A. V. & Palace Carvalho, A. Adsorption of two phenoxyacid compounds on a clay surface: A theoretical study. *Adsorption* **19**, 937–944 (2013).
54. Edet, H. O. *et al.* Heteroatoms (b, n, s) doped quantum dots as potential drug delivery system for isoniazid: Insight from dft, nci, and qtaim. *Heliyon* **9** (2023).
55. Venkataramanan, N. S. & Suvitha, A. Nature of bonding and cooperativity in linear dmso clusters: A dft, aim and nci analysis. *J. Mol. Graph. Model.* **81**, 50–59 (2018).
56. Khan, S., Sajid, H., Ayub, K. & Mahmood, T. Adsorption behaviour of chronic blistering agents on graphdiyne; excellent correlation among sapt, reduced density gradient (rdg) and qtaim analyses. *J. Mol. Liq.* **316**, 113860 (2020).
57. Torrik, A., Zaerin, S. & Zarif, M. Doxorubicin and imatinib co-drug delivery using non-covalently functionalized carbon nanotube: Molecular dynamics study. *J. Mol. Liq.* **362**, 119789 (2022).

Author contributions
Simulations were conducted by F.M.V., M.P.-N., M.R., and A.H.T. The original draft, visualizations, and writing of the main manuscript were done by F.M.V., M.R., and A.H.T. Conceptualization was done by F.M.V., M.P.-N., M.M., and A.Y.T. All authors reviewed the manuscript.

Competing interests
The authors declare no competing interests.

Additional information
Supplementary Information The online version contains supplementary material available at https://doi.org/ 10.1038/s41598-024-58347-6.

Correspondence and requests for materials should be addressed to A.T.

Reprints and permissions information is available at www.nature.com/reprints.

Publisher's note Springer Nature remains neutral with regard to jurisdictional claims in published maps and institutional affiliations.